Research Square

Preprints are preliminary reports that have not undergone peer review.
They should not be considered conclusive, used to inform clinical practice,
or referenced by the media as validated information.

Removal of phosphate from wastewater by nano-Fe3O4 modified attapulgite

Tingyu Fan

tyfan@aust.edu.cn

Anhui University of Science and Technology

Pingjuan Wu

Anhui University of Science and Technology

Changde Yang

Key Laboratory of Green Mining of Coal Resources

Peiyun Chen

Anhui University of Science and Technology

Xuyang Zhou

Anhui University of Science and Technology

Xingming Wang

Anhui University of Science and Technology

Shun Wang

Anhui University of Science and Technology

Jingkai Li

Key Laboratory of Green Mining of Coal Resources

Research Article

Keywords: attapulgite, magnetic materials, modification, nano-Fe3O4, dephosphorization

Posted Date: February 26th, 2026

DOI: https://doi.org/10.21203/rs.3.rs-8401346/v1

License: This work is licensed under a Creative Commons Attribution 4.0 International License.
Read Full License

Additional Declarations: No competing interests reported.

Removal of phosphate from wastewater by nano-Fe_3O_4 modified attapulgite

Tingyu Fan[1,2,3,*], Pingjuan Wu[1,2], Changde Yang[3], Peiyun Chen[1,2], Xuyang Zhou[1,2], Xingming Wang[1,2], Shun Wang[1,2], Jingkai Li[3]

1. School of Earth and Environment, Anhui University of Science and Technology, Huainan 232001, Anhui, China

2. State Key Laboratory for Safe Mining of Deep Coal Resources and Environment Protection, Huainan 232001, China

3. Key Laboratory of Green Mining of Coal Resources, Ministry of Education, Urumqi 830000, Xinjiang, China

---

* Corresponding author: Tingyu Fan.

E-mail: tyfan@aust.edu.cn; Tel. 0554 6631201; Fax. 0554 6631201.

Address: School of Earth and Environment, Anhui University of Science and Technology, 168 Taifeng Street, Huainan, China, 232001.

Abstract: Natural clay minerals demonstrate potential as phosphate adsorbents; however, their practical application is hindered by challenges in material recovery and limited adsorption capacity, resulting in increased operational costs. In this study, magnetic attapulgite (MATP) was synthesized using a co-precipitation method for simulating phosphate adsorption in wastewater treatment. The adsorbent was characterized using SEM, XRD, FT-IR and VSM. The characterization results confirmed the successful loading of nano Fe_3O_4 onto attapulgite (ATP). The saturation magnetization intensity of MATP achieved the threshold required for rapid solid-liquid separation and recyclability. The adsorption kinetics were best described by the pseudo-second-order model, while the adsorption isotherms followed the Langmuir model. MATP exhibited a maximum phosphate adsorption capacity of 4.83 $mg \cdot g^{-1}$, with an optimal dosage of 0.15 g and optimal performance under acidic pH conditions. The presence of Ca^{2+} in solution was found to significantly enhance the phosphate adsorption capacity of the magnetic clay composite. The phosphate adsorption process was found to be primarily governed by ligand exchange induced by -OH in MATP. This study demonstrated that magnetic reusable MATP composites have great promise for phosphorus removal and recycling.

Keywords: attapulgite, magnetic materials, modification, nano-Fe_3O_4, dephosphorization

1 Introduction

Excess phosphorus in aquatic systems induces eutrophication[1]. Algal blooms are triggered when aqueous phosphate concentrations exceed 0.02 $mg \cdot L^{-12}$. This eutrophication-driven proliferation progresses to severe aquatic ecosystem degradation [3]. Elevated phosphate levels in wastewater effluents contribute to heightened phosphorus concentrations in receiving waterbodies. Consequently, effective phosphate removal from wastewater prior to discharge constitutes a critical strategy for eutrophication mitigation.

Current phosphorus removal technologies encompass chemical precipitation[4], biological processes[5], electrocoagulation[6], membrane separation[7] and adsorption[8]. Chemical precipitation operates through the addition of metal salts to generate insoluble metal phosphates, though this approach generates substantial sludge volumes and risks secondary contamination[9]. Biological phosphorus removal operates through cellular uptake of dissolved phosphorus for polyphosphate synthesis[10], providing cost-effective operation with minimal secondary pollution, though system stability remains challenging. Electrocoagulation combines electrochemical dissolution of metal electrodes with floc formation[7]. The membrane separation method operates based on the selective permeability of semipermeable membranes for molecular phosphate separation[7, 11], offering reduced sludge production and enhanced reaction kinetics, though its operational costs remain prohibitive[12]. Adsorptive phosphorus removal utilizes porous solids with high surface areas, achieving phosphate sequestration through electrostatic interactions, ion exchange, or surface precipitation mechanisms[13].

Adsorptive phosphorus removal enables phosphorus recovery from aqueous solutions, facilitating resource recycling. Adsorption is recognized as a highly effective and cost-efficient phosphate removal strategy[14]. This method employs low-cost, non-toxic, biodegradable materials with potential reusability[15]. Material selection critically determines adsorption efficacy, with attapulgite being prioritized due to its cost-effectiveness and environmental compatibility[16]. Sustainable recyclability constitutes a key evaluation metric for adsorbent practicality. The integration of magnetic nanoparticles into water treatment systems has emerged as a research focus, particularly for enhanced solid-liquid separation[17, 18]. Fe_3O_4 nanoparticles have demonstrated superior phosphate adsorption capabilities, as extensively documented in recent studies[19-21]. However, technical complexity and elevated production costs hinder sustainable implementation at industrial scales. The incorporation of magnetic Fe_3O_4 into natural clay matrices offers cost-effective fabrication, simplified operational protocols, and enables rapid magnetic separation post-adsorption. This synergistic design allows the synthesis of regenerable adsorbents through superparamagnetic nano-Fe_3O_4 loading for multiple operational cycles[22].

The integration of magnetic nanoparticles with natural clay matrices synergistically enhances adsorption capacity, optimizes subsidence rate, and improves cost-effectiveness, providing valuable insights for aquatic eutrophication mitigation strategies. In this study, attapulgite was employed to fabricate magnetic clay composites via a co-precipitation method. The surface properties were systematically investigated to evaluate phosphate adsorption performance under varied aquatic conditions, while

the adsorption mechanisms were elucidated through integrated analyses of adsorption kinetics, isotherm models, and pre-/post-adsorption characterization.

2 Materials and Methods

2.1 Experimental materials

Attapulgite was sourced from Henan Hengyuan New Material Technology Co., Ltd. (China). All chemical reagents (analytical grade) were procured from Sinopharm Chemical Reagent Co., Ltd., China; aqueous solutions were prepared using deionized water. Potassium dihydrogen phosphate (KH_2PO_4) served as the precursor for stock solution, with pH adjustment conducted using NaOH and HCl aqueous solutions.

2.2 Preparation of MATP

Based on the method described by Chen et al [23], MATP was synthesized using a co-precipitation method. Initially, 1 g of attapulgite was added to 100 ml of pure water and ultrasonicated for 10 min to ensure complete dispersion. Subsequently, 1.96 g of $FeCl_3$-$6H_2O$ and 0.9 g of $FeCl_2$-$4H_2O$ were added to the suspension and allowed to dissolve completely. The pH of the solution was adjusted to 10 using NH_3-H_2O, followed by stirring at 60 ℃ for 3 h. The precipitated products were washed three times using ethanol and purified water and then separated using a permanent magnet. The suspension was filtered, dried at 65 ℃ for 5 h, and finally ground into a fine powder. The mass ratio of Fe_3O_4 to attapulgite in the synthesized magnetic composites was 1:1.

2.3 Characterization of the materials

The surface elemental composition of the samples was examined using a scanning electron microscope (FlexSEM 1000, Hitachi, Japan). The chemical composition of the samples was identified using an infrared spectrometer (Thermo Nicolet Nexus 670, USA) in the range of 400 - 4000 cm^{-1}. The crystal structure of the samples was determined by XRD (Bruker D8 Advance, Germany) with a scanning range of 10–70°. The magnetic properties were measured using a vibrating sample magnetometer (VSM 7040, Lake Shore, USA) to determine the values of saturation magnetization and remanent magnetization.

2.4 Batch sorption experiments

Configuration of 10 mg/L phosphate with KH_2PO_4 for subsequent MATP adsorption experiments. Unless otherwise stated, all batch experiments in this study were conducted in a solution containing 25 mL of phosphate at a concentration of 10 $mg \cdot L^{-1}$. To investigate the effect of adsorbent dosage on adsorption, phosphate adsorption experiments were performed by adding 0.05–0.5 g of adsorbent to the phosphorus-containing wastewater. To explore the effect of pH on adsorption, experiments were conducted at pH values ranging from 2 to 10. To evaluate the effect of different Ca^{2+} concentrations on adsorption, 1 mL of Ca^{2+} solution with concentrations ranging from 10 to 160 $mg \cdot L^{-1}$ was added to the phosphate solution.

2.5 Recyclable and regenerated performance

To evaluate the recyclable and regenerative properties of the adsorbents, recycling experiments were conducted. After filtering the adsorbed material, pure water was

added, followed by 5 minutes of sonication and 5 minutes of centrifugation; the supernatant was then decanted. After repeating the above steps three times, the material was dried at 65 ℃ for subsequent experimental cycles. In this study, four consecutive adsorption-desorption cycles were performed.

2.6 Analytical methods

The phosphate concentration was determined using a Mo-Sb anti-spectrophotometer (GB 11893-89). The phosphate removal rate (Eq. 1) and phosphate adsorption capacity (Eq. 2) were calculated[24].

$$R = \frac{C_0 - C_1}{C_0} \times 100\,\% \quad (1)$$

$$Q_e = \frac{(C_0 - C_1)V}{m} \quad (2)$$

Where $R$is the phosphate removal rate (%); C_0 and C_1 are the initial concentration of the phosphate solution and the concentration after adsorption ($mg \cdot L^{-1}$), respectively; Q_e is the phosphate adsorption capacity ($mg \cdot g^{-1}$); V is the solution volume (L) and m is the adsorbent mass (g).

The pseudo-first-order model (Eq. 3), pseudo-second-order model (Eq. 4), Elovich model (Eq. 5), and intraparticle diffusion model (Eq. 6) were used to fit the experimental data[25, 26].

$$\text{Pseudo-first-order model:}\quad \ln(Q_e - Q_t) = \ln Q_e - k_1 t \quad (3)$$

$$\text{Pseudo-second-order model:}\quad \frac{t}{Q_t} = \frac{1}{k_2 Q_e^2} + \frac{t}{Q_e} \quad (4)$$

$$\text{Elovich model:}\quad Q_t = \frac{1}{a}\ln ab + \frac{1}{a}\ln t \quad (5)$$

$$\text{Intraparticle diffusion model:}\quad Q_t = c + t^{0.5}K_{td} \quad (6)$$

where Q_e and Q_t are the amount of phosphate adsorbed ($mg \cdot g^{-1}$) at equilibrium

and at time t, respectively. k_1, k_2, and K_{td} are the equilibrium rate constants.

To further analyze the adsorption mechanism, adsorption isotherm models, including the Langmuir model (Eq. 7), Freundlich model (Eq. 8), and Temkin model (Eq. 9)[27].

$$\text{Langmuir: } Q_e = \frac{Q_{max} K_l C_e}{1 + K_l C_e} \tag{7}$$

$$\text{Freundlich: } Q_e = K_f C_e^{\frac{1}{n}} \tag{8}$$

$$\text{Temkin: } Q_e = B_T \ln A_T + B_T \ln C_e \tag{9}$$

Where K_l is Langmuir's constant, L·mg^{-1}; K_f is Freundlich's constant, which is related to the adsorption capacity and adsorption strength; T is the absolute temperature (K), R is the universal gas constant (8.314 J·mol^{-1}·K^{-1}), B_T is the heat of adsorption, and A_T is the equilibrium binding constant (L·min^{-1}), which corresponds to the maximum binding energy [27].

3 Results

3.1 Adsorbent characterization

3.1.1 SEM characterization analysis

Fig. 1 showed the morphological comparison of ATP and MATP. It can be observed that ATP exhibits a typical lamellar or tubular flake morphology. In addition, it can be observed that a large number of nanoscale Fe_3O_4 particles are uniformly distributed on the surface of MATP. These results preliminarily demonstrate the successful synthesis of the magnetic nanomaterial in this study.

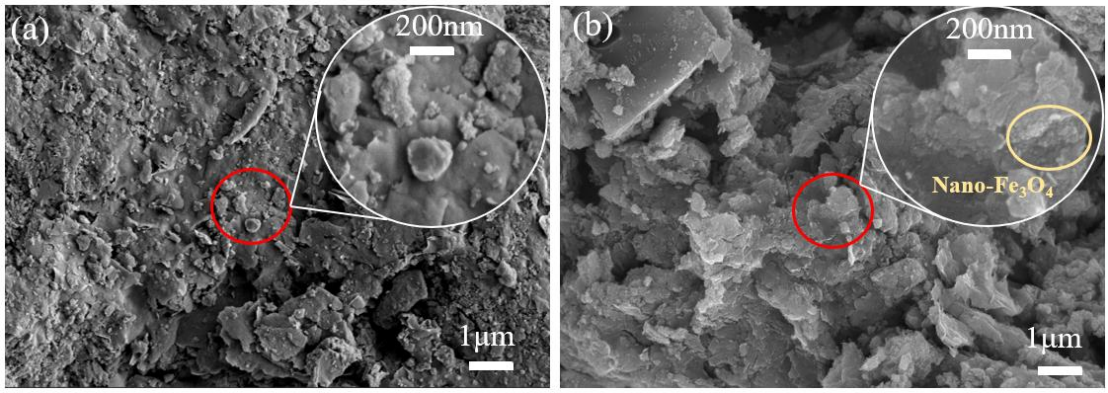


Fig. 1. SEM image of ATP and MATP

(a) ATP; (b) MATP

3.1.2 FTIR characterization analysis

The FTIR spectra of ATP and MATP are shown in Fig. 2. In the infrared spectrum of ATP, the peak at 3635 cm^{-1} was attributed to the stretching vibrations of Mg–OH and Al–OH[28]. The band at 3442 cm^{-1} corresponded to physically adsorbed water, while the peak at 1631 cm^{-1} was ascribed to the –OH stretching vibration in attapulgite[16]. The peaks at 1039 cm^{-1} and 876 cm^{-1} were attributed to the stretching vibrations of Si–O–Si and Si–OH groups in ATP, whereas the peak at 792 cm^{-1} corresponded to the bending vibration of Si–O–Si in ATP[16, 29]. The peak intensity in MATP was reduced; however, a characteristic peak appeared at 560 cm^{-1}, which was attributed to the stretching mode of Fe–O in Fe_3O_4. This confirmed the successful deposition of Fe_3O_4 on ATP, consistent with the XRD results[29]. The characteristic peaks of ATP were retained in MATP, indicating that the modification did not alter the original structure of the material.

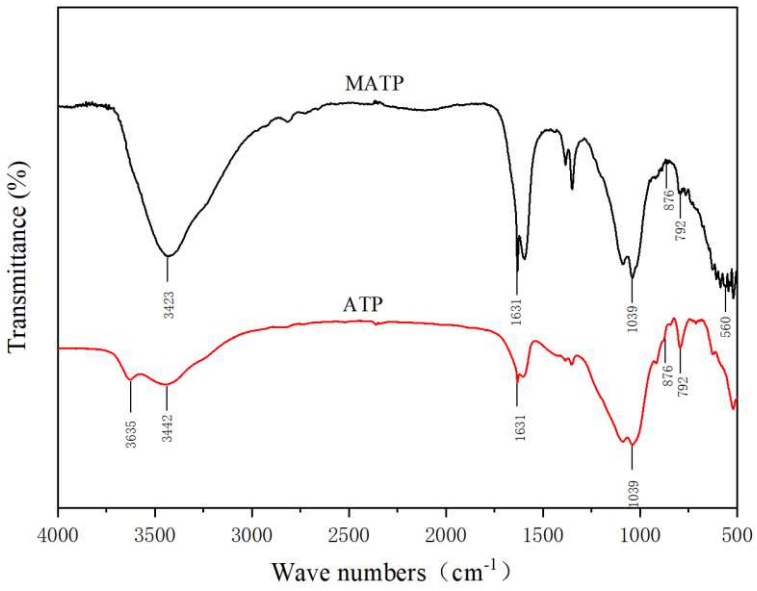


Fig. 2. Fourier infrared spectra of ATP and MATP

3.1.3 XRD characterization analysis

The XRD diffractograms of ATP and MATP are shown in Fig. 3. The XRD patterns showed that ATP exhibited predominantly SiO_2 diffraction peaks (JCPDS card No. 46-1045), indicating that the SiO_2 in the sample had high crystallinity[30]. Additionally, impurity minerals such as carbonates were identified alongside quartz. The XRD pattern of MATP displayed additional characteristic peaks corresponding to Fe_3O_4 (JCPDS card No. 19-0629), confirming the successful loading of Fe_3O_4 onto ATP[31]. In general, MATP retained the characteristic mineral composition of ATP. Furthermore, the formation of numerous nanoparticles with high specific surface area led to broader diffraction peaks. The diffraction peaks of MATP showed no significant changes compared to those of ATP, demonstrating that the Fe_3O_4 modification process did not alter the material's structure.

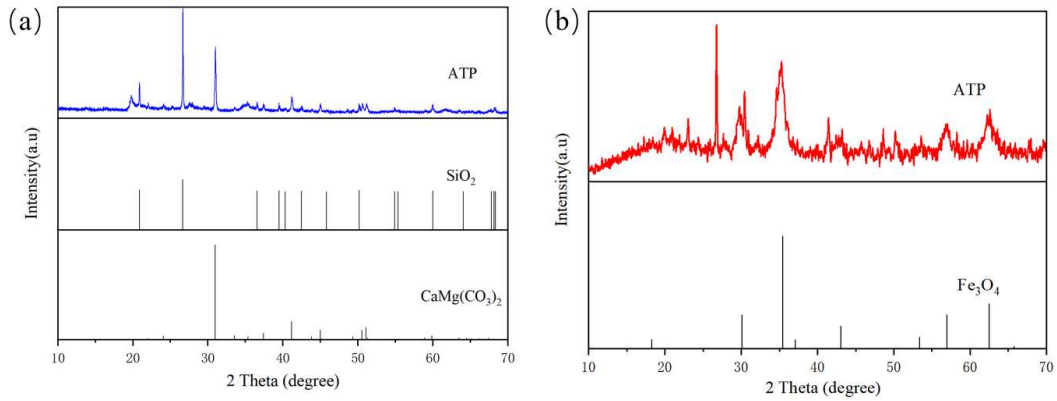


Fig. 3. XRD diffraction patterns of ATP and MATP

(a) ATP; (b) MATP

3.1.4 VSM characterization analysis

Fig. 4 displayed the magnetic hysteresis loop of MATP. The saturation magnetization (Ms) of MATP was measured as 9.09 emu·g^{-1} with a coercivity (Hc) of 4.05 Oe. The S-shaped hysteresis curve originating at zero field exhibited negligible hysteresis, with both coercivity and remanent magnetization approaching zero, confirming the superparamagnetic behavior of the material[32]. This property ensured effective dispersion in aqueous solutions without external magnetic fields, preventing particle aggregation. The saturation magnetization value satisfied the minimum requirements for solid-liquid separation and material recovery[33].

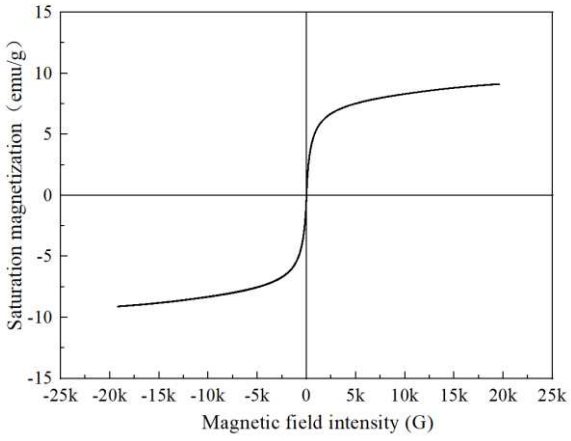


Fig. 4. Magnetic hysteresis loop of MATP

3.2 Factors affecting adsorption

3.2.1 Adsorbent dose

As depicted in Fig. 5a, the phosphate removal efficiency of MATP exhibited rapid enhancement within the low dose range (0.05–0.10 g). When the dosage exceeded 0.10 g, the removal efficiency showed a reduced growth rate. At 0.05 g dosage, the adsorption capacity per unit mass decreased, suggesting that the available adsorption sites and functional groups increased proportionally with adsorbent quantity. At 0.15 g dosage, MATP achieved 95.75% phosphate removal efficiency, demonstrating effective phosphate elimination from aqueous systems. Considering both economic feasibility and removal performance, the optimal MATP dosage was determined to be 0.15 g.

3.2.2 pH

The phosphate removal efficiency of MATP was evaluated across varying pH conditions, along with the zeta potential values of ATP before and after modification (Fig. 5b). MATP exhibited higher zeta potential values compared to ATP, resulting in enhanced phosphate adsorption. Solution pH was found to govern the surface charge distribution of the adsorbent and the competitive adsorption between OH^- and phosphate ions. Under acidic conditions (pH < 7), the adsorbent surface acquired stronger positive charges, leading to enhanced phosphate adsorption. With increasing pH (>7), the dominant phosphate species shifted from HPO_4^{2-} to PO_4^{3} [34]. The zeta potential gradually decreased with pH elevation, reducing the adsorbent's capacity to capture phosphate ions. The phosphate removal efficiency exhibited a non-monotonic

trend, initially decreasing before showing subsequent improvement.

3.2.3 Ca^{2+} concentration

In aqueous systems, phosphate adsorption is influenced by coexisting ions that may exert synergistic or antagonistic effects[35]. Ca^{2+} promotes phosphate adsorption via formation of ternary surface complexes (metal-P-Ca)[36]. $CaCl_2$ was introduced into the phosphate solution to evaluate the impact of cationic interactions on adsorption performance. The Ca^{2+} concentration-dependent adsorption behavior of MATP was demonstrated in Fig. 5c. Phosphate adsorption capacity showed progressive enhancement with elevated Ca^{2+} concentrations, reaching saturation at approximately 80 $mg \cdot L^{-1}$. At saturation conditions, the adsorption capacity demonstrated a 12.87% enhancement relative to the Ca^{2+} free system.

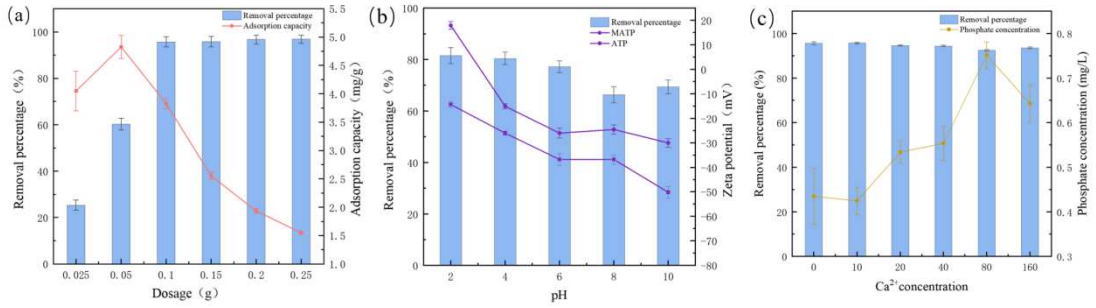


Fig. 5. Effect of various factors on the removal phosphate

(a) Dosage. Initial phosphate concentration: 10 $mg \cdot L^{-1}$; initial pH:7; reaction time: 3 hr. (b) Initial pH. initial phosphate concentration: 10 $mg \cdot L^{-1}$; material dosage: 0.15 g; reaction time: 3 hr. (c) Ca^{2+} concentration. Initial phosphate concentration: 10 $mg \cdot L^{-1}$; initial pH:7; material dosage: 0.15 g; reaction time: 3 hr.

3.3 Adsorption kinetics

The kinetic adsorption data of MATP were fitted with pseudo-first-order and pseudo-second-order models (Fig. 6), with corresponding parameters summarized in

Table 1. The pseudo-second-order model provided a superior fit (R^2= 0.999) compared to the pseudo-first-order model, as evidenced by its proximity to unity. This suggests the adsorption process was predominantly chemisorption-mediated, with physical adsorption playing a secondary role, indicating surface-active site-dependent kinetics[36].

The Elovich model parameters revealed that diffusion contributed to the rate-limiting process, while chemisorption played a dominant role in the adsorption kinetics[37]. The intra-particle diffusion model was employed to elucidate the rate-controlling mechanisms, providing detailed insights into the adsorption process[38, 39]. As shown in Fig. 6d, the adsorption process exhibited two distinct phases. The first stage demonstrated a higher correlation coefficient (R^2) and greater intraparticle diffusion rate constant (kp1 > kp2). This suggested rapid initial adsorption followed by decreased kinetics in the second stage, attributed to progressive saturation of active sites[40].

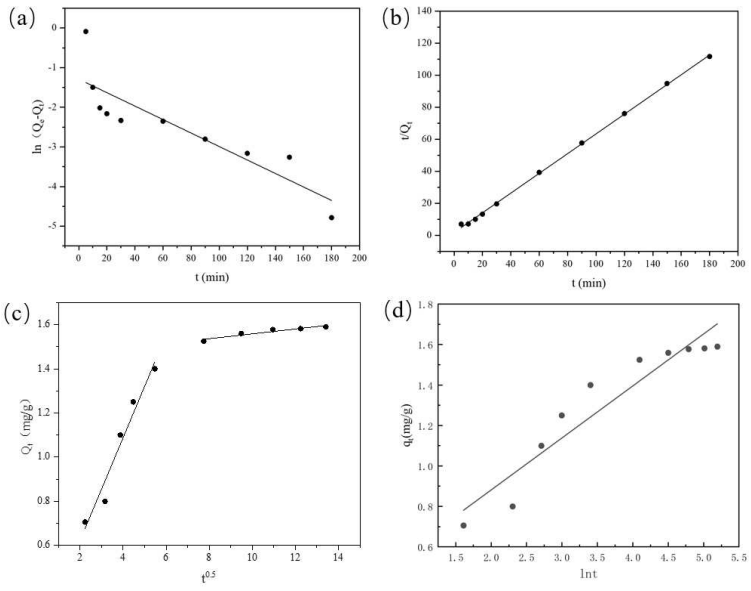


Fig. 6. Four linear kinetic models for the adsorption of phosphate on MATP. Initial phosphate concentration: 10 mg·L^{-1}; initial pH:7; material dosage: 0.2 g; reaction time: 0-3 hr. (a) Pseudo-first-order kinetic model; (b) Pseudo-second-order kinetic model; (c) Elovich model; (d) Intraparticle diffusion model.

Table 1 Adsorption kinetic parameters of phosphate on MATP

Adsorbent type	Parameters	
Pseudo-first-order	Q_e (mg·g^{-1})	0.275
	k_1	0.017
	R^2	0.778
Pseudo-second-order kinetic model	Q_e (mg·g^{-1})	1.625
	k_2	1.437
	R^2	0.999
Elovich model	a	3.89
	b	1.08
	R^2	0.901
Intraparticle diffusion model	c_1	0.086
	K_{td1}	0.256
	R_1^2	0.905
	c_2	1.321
	K_{td2}	0.022
	R_2^2	0.771

3.4 Adsorption isotherms

The isotherm fitting parameters and figure for Langmuir, Freundlich, and Temkin models were summarized in Table 2 and Fig.7,respectively. The Langmuir model achieved a higher determination coefficient (R^2 = 0.986) compared to the Freundlich model (R^2=0.966). Visual inspection of the fitted curves confirmed the superior fitting performance of the Langmuir model. This suggested monolayer adsorption through chemisorption-driven mechanisms. The calculated maximum adsorption capacity reached 4.83 mg·g^{-1}. The Freundlich model indicated potential multilayer adsorption on heterogeneous surfaces. This implied coexisting multilayer adsorption mechanisms,

revealing multifaceted adsorption characteristics. The Temkin model showed satisfactory fitting (R^2=0.890), further validating chemisorption dominance in the magnetic composite system.

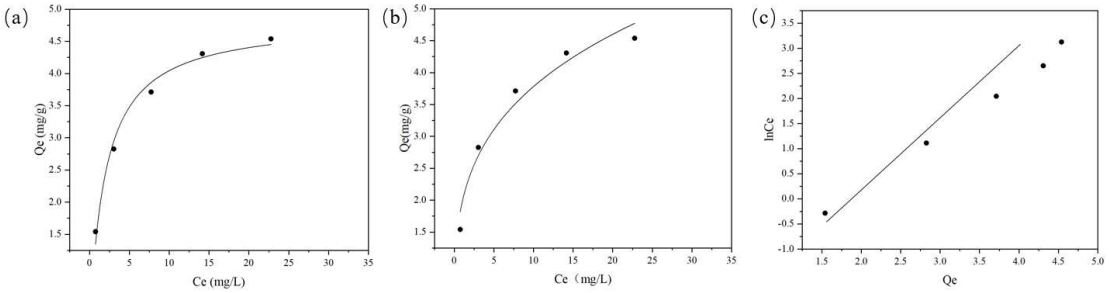


Fig. 7. Three models for the adsorption of isotherms of MATP on phosphate (a) Langmuir model；(b) Freundlich model；(c) Temkin model. Initial phosphate concentration: 10-50 mg·L^{-1}; initial pH:7; material dosage: 0.15 g; reaction time: 3 hr.

Table 2 The fitting results of isothermal equation of three models of MATP

Adsorbent type	Langmuir model			Freundlich model			Temkin model
Parameters	K_l	Q_{max}	R^2	K_f	n	R^2	R^2
	0.515	4.830	0.986	1.971	3.534	0.966	0.890

3.5 Recycling experiments

Regeneration capability represents a critical indicator for evaluating adsorbent performance[41]. Four consecutive adsorption-desorption cycles were conducted to assess MATP's regeneration performance (Fig. 8). The observed efficiency decline was attributed to incomplete phosphate desorption, whereby residual ions occupied active sites on the magnetic composite surface, thereby impairing subsequent adsorption[42, 43]. After four-cycle regeneration, MATP retained 76.14% phosphate removal efficiency, demonstrating practical reusability and offering economic advantages for water treatment applications.

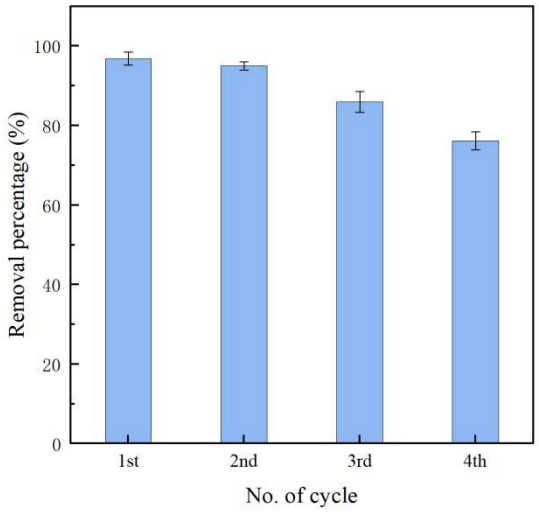


Fig. 8. The effect of MATP cycle times on phosphate removal efficiency. Initial phosphate concentration: 10 mg·L^{-1}; initial pH:7; material dosage: 0.15 g; reaction time: 3 hr.

4 Discussion

4.1 Structure of MATP

Attapulgite (ATP), a hydrated magnesium aluminum silicate mineral, features a 2:1 layered structure with parallel band arrangements. Previous studies demonstrated that Ca^{2+} in ATP facilitates phosphorus removal through precipitation with PO_4^{3-}[35]. However, natural clay minerals exhibit limited phosphate adsorption capacity in aqueous systems due to their inherent structural constraints[31]. This limitation originates from the net negative charge distribution within their crystalline frameworks. The incorporation of Fe_3O_4 nanoparticles enables surface charge reversal, effectively enhancing phosphate adsorption capacity in magnetic composites[44].

In this study, cost-effective attapulgite served as the substrate for synthesizing MATP through coprecipitation method. Comprehensive characterization analyses verified the successful integration of Fe_3O_4 nanoparticles onto the attapulgite matrix. The measured

saturation magnetization (9.09 emu·g^{-1}) confirmed excellent magnetic responsiveness, enabling rapid solid-liquid separation under external magnetic fields for adsorbent recovery.

4.2 Adsorption conditions impact

The density of accessible adsorption sites exhibits progressive augmentation with increasing dosage within the low dosage range[45]. However, the specific adsorption capacity per unit mass showed a declining trend at higher dosages, attributed to overlapping effective adsorption sites[46]. This suggests that overdosing beyond the optimal level induces site saturation and diminished adsorption efficiency, leading to inefficient resource allocation.

As shown in Fig. 5b, the inherent negative surface charge of attapulgite hinders electrostatic adsorption of anionic phosphate species. Solution pH critically influences phosphate adsorption by modulating both MATP's surface charge and phosphate speciation. Phosphate exists predominantly as $H_2PO_4^-$ (pH 2-7) and HPO_4^{2-} (pH 7-10), with divergent adsorption affinities between these species[47]. Under acidic conditions, MATP's positive surface charge promotes electrostatic interactions with $H_2PO_4^-$ anions[48]. This charge complementarity enhances $H_2PO_4^-$ adsorption through favorable electrostatic forces. Under alkaline conditions, both MATP and dominant HPO_4^{2-} species carry negative charges[48]. This charge similarity induces interionic repulsion, significantly diminishing adsorption capacity. Comparable charge-dependent adsorption mechanisms are well documented in related studies[49-51]. At pH 8, OH^- ions compete with phosphate for adsorption sites, further diminishing removal efficiency[45].

The influence of Ca^{2+} coexisting ions on adsorption behavior was investigated. The introduction of Ca^{2+} augmented surface positive charge of the magnetic composite, thereby promoting electrostatic attraction with phosphate anions. Furthermore, Ca^{2+} facilitates the formation of $CaHPO_4$ precipitates that subsequently adsorb onto the composite surface, thereby synergistically improving adsorption capacity.

4.3 Adsorption model fit

To elucidate the phosphate adsorption mechanism, kinetic and isothermal adsorption analyses were conducted. Kinetic analysis confirmed the predominance of chemisorption in MATP's phosphate adsorption mechanism. These findings align with established adsorption mechanisms reported in clay-based systems[34, 52, 53]. The experimental data exhibited superior alignment with the Langmuir model (R^2=0.9858), indicating homogeneous monolayer adsorption with uniformly distributed active sites[54]. The observed correlation between kinetic parameters and regeneration efficiency suggests that incomplete regeneration compromises subsequent adsorption capacity. This phenomenon stems from the pseudo-second-order kinetic principle, where adsorption rate depends on the square of available active sites[55]. MATP was increased from 0.17 $mg \cdot g^{-1}$ to 4.83 $mg \cdot g^{-1}$ compared to the pre-modified ATP, demonstrating significant performance improvement[56].

4.4 Adsorption mechanism

Fig. 9 presented comparative SEM micrographs of ATP and phosphate-laden MATP, revealing distinct surface morphology evolution. Post-adsorption

characterization revealed surface smoothening and densification, attributed to phosphate deposition and diminished interparticle porosity. These morphological transformations confirm effective phosphate immobilization through surface complexation mechanisms.

FT-IR analysis was performed to investigate functional group modifications during phosphate adsorption (Fig. 10a). The characteristic FT-IR peaks of MATP remained largely unaltered post-adsorption compared to the pristine material. Emerging absorption bands at 2949 cm^{-1} and 2919 cm^{-1} (absent in pristine MATP) correspond to C-H stretching vibrations of $-CH_3$ and $-CH_2$ groups[57]. A new vibrational mode appeared at 626 cm^{-1}, assigned to O-P-O bending vibrations, confirming inner-sphere complexation through ligand exchange mechanisms[58].

XPS analysis was performed to investigate the phosphate adsorption mechanism through comparative spectral analysis. As shown in Fig. 10b, the XPS results reveal a clear P 2p peak at a binding energy of 132.32 eV, confirming the effective adsorption of phosphate onto the material. Fig. 10c showed that the Fe 2p spectrum exhibited characteristic doublets at 710.6 eV ($Fe\ 2p_{1/2}$) and 724.6 eV ($Fe\ 2p_{3/2}$). Post-adsorption Fe 2p peaks underwent positive binding energy shifts, suggesting Fe–O–P bond formation through electron transfer (Fig. 10d) [59]. These results demonstrate that the chemical binding between iron and phosphate plays an important role in the adsorption process.

After adsorption, the percentage of Fe-O peak area decreased from 7.94% to 6.17%, which may be due to the formation of Fe-P compounds leading to the occupation

of metal binding site by P. The adsorption of phosphorus on the surface was also observed in the presence of hydroxyl oxygen, which is the most important component of phosphorus. The hydroxyl oxygen content on the surface decreased from 43.34% to 39.37% after adsorption, which proved that hydroxyl oxygen was involved in the adsorption of phosphorus and may form Fe-O-P coordination complexes with phosphate exchange ligands in water[12].

Fig. 11 schematically illustrates the dominant phosphate adsorption mechanisms of MATP. The -OH induced ligand exchange in MATP dominates phosphate adsorption and gives rise to complexation phenomena. In particular, the protonated metal hydroxyl groups adsorbed phosphate by electrostatic attraction when the pH was acidic.

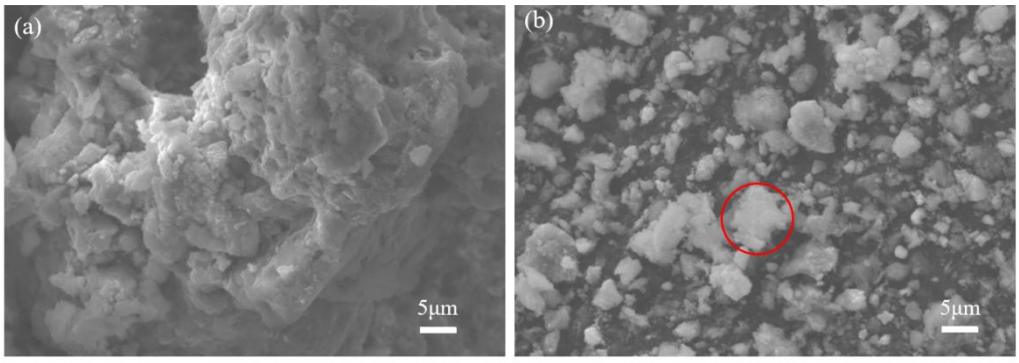
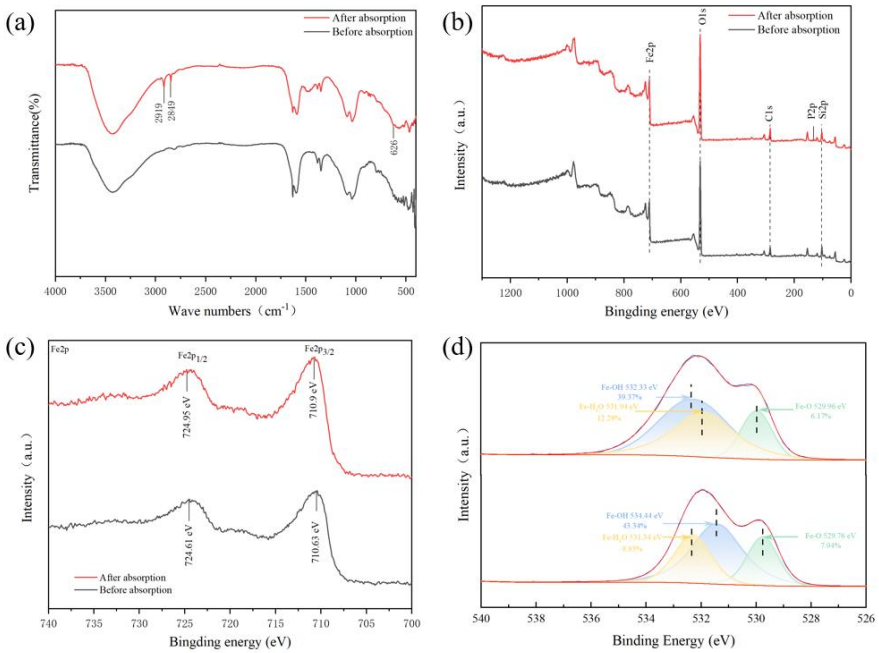


Fig. 9. SEM images of MATP before and after adsorption phosphate

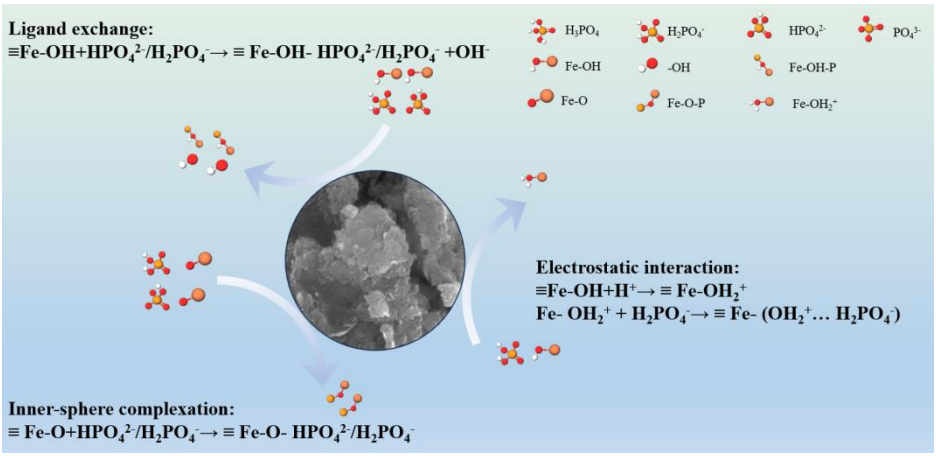
(a) before adsorption; (b) after adsorption



389

390 **Fig. 10.** (a) FT-IR spectra, (b) XPS spectra of Full spectrum, (c) Fe 2p and (d) O 1s for MATP

391 before and after phosphate adsorption.



392

393 **Fig. 11.** Main mechanisms for phosphate adsorption by MATP

394 ## 5 Conclusions

395 To address phosphate-induced eutrophication, magnetic attapulgite composites

396 (MATP) were successfully synthesized via co-precipitation. Systematic investigations

397 encompassing material characterization, adsorption optimization, and mechanistic

398 analysis yielded the following key findings:

399 (1) MATP was successfully synthesized via co-precipitation, with SEM, FTIR, and

XRD confirming homogeneous dispersion of Fe_3O_4 nanoparticles on attapulgite surfaces while preserving its native mineral structure. Magnetic hysteresis loops confirmed superparamagnetic behavior (S-type loops), enabling rapid solid-liquid separation under external magnetic fields.

(2) Batch experiments identified optimal parameters: 0.15 g adsorbent dosage and acidic pH conditions. Calcium ion co-presence enhanced adsorption capacity through synergistic effects. MATP demonstrated notable regenerability, maintaining 76.14% phosphate removal efficiency after four adsorption-desorption cycles.

(3) The adsorption process was consistent the Langmuir model with a maximum adsorption capacity of 4.83 $mg \cdot g^{-1}$. Remarkably, the adsorption of phosphate by MATP can be attributed to ligand exchange, inner-sphere complexation and electrostatic attraction.

Declarations

Ethical Approval

Not applicable.

Consent to Participate

The authors have approved the final draft of the manuscript.

Data Availability

The datasets used and/or analyzed during the current study are available from the corresponding author on reasonable request.

Conflict of interest

The authors have no competing interests to declare that are relevant to the content of this article.

Funding

This work was supported by the Natural Science Research Project of Anhui Provincial Colleges and Universities (2023AH051225); Scientific research project of Yushu Collar Coal Mine of Yuneng Xinjiang Investment Group (2021xgyh092212);Jianghuai Talent Cultivation Program Innovation Team(Document No. Wanzuobanzi [2025] 16)

Author Contributions

Tingyu Fan: Writing – review & editing, Writing – original draft, Visualization, Validation, Supervision, Software, Project administration, Methodology, Investigation, Formal analysis, Data curation.Funding acquisition, Conceptualization. **Pingjuan Wu:**Writing – review & editing, Writing – original draft, Validation, Supervision,

Software, Methodology, Investigation, Formal analysis, Data curation. Resources, Methodology, Investigation. **Changde Yang:** Writing – review & editing, Writing – original draft, Resources, Project administration, Funding acquisition.**Peiyun Chen:** Writing – review & editing, Writing – original draft,Formal analysis, Data curation. **Xuyang Zhou :**Writing – review & editing, Writing – original draft, Formal analysis, Data curation.**Xingming Wang :** Writing – review & editing, Writing – original draft, Validation, Supervision, Investigation, Formal analysis. **Shun Wang:** Writing – review & editing, Writing – original draft, Formal analysis, Data curation. **Jingkai Li:** Writing – review & editing, Writing – original draft, Formal analysis, Data curation.

References

(1) Huo J.; Min X.; Wang Y. Zirconium-modified natural clays for phosphate removal: Effect of clay minerals[J]. *Environ Res*, 2021, 194: 110685.

(2) Duan X.; Zhao Y Y.; Zhang J C. Characteristics of the root exudate release system of typical plants in plateau lakeside wetland under phosphorus stress conditions[J]. *Open Chemistry*, 2020, 18(1): 808-821.

(3) Geletu T T. Lake eutrophication: Control of phytoplankton overgrowth and invasive aquatic weeds[J]. *Lakes & Reservoirs: Research & Management*, 2023, 28(1): e12425.

(4) Perera M K.; Englehardt J D.; Cohn J L.; Dauer E A.; Shukla D. Electrohydromodulation for phosphate recovery from wastewater[J]. *Separation Purification Technology*, 2020, 247: 116909.

(5) Zhou Q.; Sun H.; Jia L.; Wu W.; Wang J. Simultaneous biological removal of nitrogen and phosphorus from secondary effluent of wastewater treatment plants by advanced treatment: A review[J]. *Chemosphere*, 2022, 296: 134054.

(6) Ren Y.; Zheng W.; Duan X.; Goswami N.; Liu Y. Recent advances in electrochemical removal and recovery of phosphorus from water: A review[J]. *Environmental Functional Materials*, 2022, 1(1): 10-20.

(7) Li X.; Shen S.; Xu Y.; Guo T.; Dai H.; Lu X. Application of membrane separation processes in phosphorus recovery: A review[J]. *Sci Total Environ*, 2021, 767: 144346.

(8) Awual M R. Efficient phosphate removal from water for controlling eutrophication using novel composite adsorbent[J]. *Journal of Cleaner Production*, 2019, 228: 1311-1319.

(9) Wang L K.; Wang M H S.; Shammas N K.; Hahn H H. Physicochemical treatment consisting of chemical coagulation, precipitation, sedimentation, and flotation[J]. *Integrated natural resources research*, 2021: 265-397.

(10) Zahed M A.; Salehi S.; Tabari Y.; Farraji H.; Ataei-Kachooei S.; Zinatizadeh A A.; Kamali N.; Mahjouri M. Phosphorus removal and recovery: state of the science and challenges[J]. *Environmental Science and Pollution Research*, 2022, 29(39): 58561-58589.

(11) Li X.; Shen S.; Xu Y.; Guo T.; Dai H.; Lu X. Application of membrane separation processes in phosphorus recovery: A review[J]. 2021, 767: 144346.

(12) Zhang Y.; Li Y.; Chen Z.; Qin J.; Chen Y.; Li J.; Wang Z.; Li B.; Wang X. Preparation of Fe/Zr bimetallic oxide beads and its performance and mechanism for advanced treatment of actual phosphorus-containing wastewater[J]. *Journal of Water Process Engineering*, 2023, 55: 104186.

(13) Recepoglu Y K.; Goren A Y.; Orooji Y.; Khataee A. Carbonaceous materials for removal and recovery of phosphate species: Limitations, successes and future improvement[J]. *Chemosphere*, 2022, 287: 132177.

(14) Wang S.; Huang Y.; Wu Q.; Yao W.; Lu Y.; Huang B.; Jin R. A review of the application of iron oxides for phosphorus removal and recovery from wastewater[J]. *Critical Reviews in Environmental Science Technology*, 2024,

54(5): 405-423.
(15) Bacelo H.; Pintor A M A.; Santos S C R.; Boaventura R A R.; Botelho C M S. Performance and prospects of different adsorbents for phosphorus uptake and recovery from water[J]. *Chem Eng J*, 2020, 381: 122566.
(16) Cui X.; Zhong Z.; Xie X.; Jiang P. Sorptive removal of cadmium using the attapulgite modified by the combination of calcination and iron[J]. *Environmental Science and Pollution Research*, 2023, 30(57): 120820-120831.
(17) Yin Q.; Ren H.; Wang R.; Zhao Z. Evaluation of nitrate and phosphate adsorption on Al-modified biochar: Influence of Al content[J]. *Sci Total Environ*, 2018, 631: 895-903.
(18) Jack J.; Huggins T M.; Huang Y.; Fang Y.; Ren Z J. Production of magnetic biochar from waste-derived fungal biomass for phosphorus removal and recovery[J]. *Journal of Cleaner Production*, 2019, 224: 100-106.
(19) Samaraweera H.; Zahir A.; Alam S S.; Perera S S.; Masud M A A.; Khan A H.; Oguntuyi D O.; Yunusu W.; Shin W S.; Mohamed M M. Sustainable utilization of Fe_3O_4-modified activated lignite for aqueous phosphate removal and ANN modeling[J]. *Environ Res*, 2024, 260: 119618.
(20) Li G.; Zhang Y.; Hu X.; Wei T.; Li J.; Hongbin W.; Wang X. A study on the performance of a recyclable adsorbent La@Fe for phosphate adsorption in wastewater[J]. *Process Safety Environmental Protection*, 2024, 188: 25-38.
(21) Wang G.; Liu R.; Yang Z.; Liu W.; Xu X.; Zhang S.; Cheng Z.; Lv G.; Xu C.; Cai J. Enhanced simultaneous removal of phosphate and ammonium from swine wastewater using magnetic magnesium–loaded Chinese herbal medicine residues: Performance, mechanism, and resource utilization[J]. *Bioresour Technol*, 2024, 393: 130103.
(22) Song Q.; Huang S.; Xu L.; Wang N.; Hu Z.; Luo X.; Zheng Z. Synthesis of magnetite/lanthanum hydroxide composite and magnetite/aluminum hydroxide composite for removal of phosphate[J]. *Sci Total Environ*, 2020, 723: 137838.
(23) Chen L.; Wu X.; Liu C.; Zhao Y.; Huang Q. Study on removal of Microcystis aeruginosa and Cr (VI) using attapulgite-Fe_3O_4 magnetic composite material (MCM)[J]. *Algal Research*, 2021, 60: 102501.
(24) Seliem M K.; Komarneni S.; Byrne T.; Cannon F S.; Shahien M G.; Khalil A A.; El-Gaid I M A. Removal of perchlorate by synthetic organosilicas and organoclay: Kinetics and isotherm studies[J]. *Applied Clay Science*, 2013, 71: 21-26.
(25) Yang Y.; Hou J.; Wang P.; Wang C.; Miao L.; Ao Y.; Xu Y.; Wang X.; Lv B.; You G. Interpretation of the disparity in harvesting efficiency of different types of Microcystis aeruginosa using polyethylenimine (PEI)-coated magnetic nanoparticles[J]. *Algal Research*, 2018, 29: 257-265.
(26) Kusuma H S.; Amenaghawon A N.; Darmokoesoemo H.; Neolaka Y A B.; Widyaningrum B A.; B C L A.; Orukpe P I. Evaluation of extract of Ipomoea batatas leaves as a green coagulant–flocculant for turbid water treatment: Parametric modelling and optimization using response surface methodology and artificial neural networks[J]. *Environmental Technology & Innovation*,

2021, 24: 102005.
(27) Zheng L.; Yang Y.; Meng P.; Peng D. Absorption of cadmium (II) via sulfur-chelating based cellulose: characterization, isotherm models and their error analysis[J]. *Carbohydr Polym*, 2019, 209: 38-50.
(28) Guo H.; Xia K.; Cao M.; Zhang X. Surface Modification of Attapulgite by Grafting Cationic Polymers for Treating Dye Wastewaters[J]. *Materials*, 2021, 14(4).
(29) Shabani E.; Salimi F.; Jahangiri A. Removal of Arsenic and Copper from Water Solution Using Magnetic Iron/Bentonite Nanoparticles (Fe_3O_4/Bentonite)[J]. *Silicon*, 2019, 11(2): 961-971.
(30) Hao Z.; Zhou J.; Liu D.; Zhang Z.; Zhang T.; Sun J.; Xu J.; Yang N.; Wu H. Two-dimensional confinement engineering of SiO_2 nanosheets supported nano-cobalt for high-efficiency microwave absorption[J]. *Chem Eng J*, 2023, 473: 145296.
(31) Lu Z.; Zhang K.; Liu F. Simultaneous recovery of ammonium and phosphate from aqueous solutions using Mg/Fe modified NaY zeolite: Integration between adsorption and struvite precipitation[J]. *Separation Purification Technology*, 2022, (299): 121713.
(32) Fan L.; Du B.; Pei F.; Hu W.; Guo A.; Xie Z.; Liu B.; Tong Z.; Mu X.; Tan W. Surface plasmon resonance sensor based on core-shell Fe_3O_4@ SiO_2@ Au nanoparticles amplification effect for detection of T-2 toxin[J]. *Sensors*, 2023, 23(6): 3078.
(33) Fan L.; Luo C.; Lv Z.; Lu F.; Qiu H. Removal of Ag^+ from water environment using a novel magnetic thiourea-chitosan imprinted Ag^+[J]. *J Hazard Mater*, 2011, 194: 193-201.
(34) Wu S F.; Cheng H M. Adsorptive Removal of Phosphate from Water Using Aluminum Terephthalate (MIL-53) Metal–Organic Framework and Its Hollow Fiber Module[J]. *Recycling*, 2024, 9.
(35) Xu C.; Feng Y.; Li H.; Yang Y.; Wu R. Adsorption and immobilization of phosphorus from eutrophic seawater and sediment using attapulgite-Behavior and mechanism[J]. *Chemosphere*, 2023, 313: 137390.
(36) Xue Y.; Xiang P.; Jiang Y.; Lian H.; Mo J.; Li M. Influence of Ca^{2+} on phosphate removal from water using a non-core-shell Fe_3O_4@ ZIF-67 composites[J]. *Journal of Environmental Chemical Engineering*, 2020, 8(5): 104458.
(37) Garg R.; Garg R.; Sillanpää M.; Alimuddin.; Khan M A.; Mubarak N M.; Tan Y H. Rapid adsorptive removal of chromium from wastewater using walnut-derived biosorbents[J]. *Scientific Reports*, 2023, 13(1): 6859.
(38) Ahmed M J.; Theydan S K. Adsorption of p-chlorophenol onto microporous activated carbon from Albizia lebbeck seed pods by one-step microwave assisted activation[J]. *Journal of Analytical Applied Pyrolysis*, 2013, 100: 253-260.
(39) Theydan S K.; Ahmed M. Adsorption of methylene blue onto biomass-based activated carbon by FeCl3 activation: Equilibrium, kinetics, and thermodynamic studies[J]. *Journal of Analytical Applied Pyrolysis*, 2012, 97:

116-122.
(40) Dehmani Y.; Sellaoui L.; Alghamdi Y.; Lainé J.; Badawi M.; Amhoud A.; Bonilla-Petriciolet A.; Lamhasni T.; Abouarnadasse S. Kinetic, thermodynamic and mechanism study of the adsorption of phenol on Moroccan clay[J]. *J Mol Liq*, 2020, 312: 113383.
(41) Liu S.; Zhao S.; Fan F Q.; Zhang B T.; Wang S R. Magnetically separable and recyclable lanthanum/iron co-modified attapulgite: A sustainable option to efficiently control phosphate loading[J]. *Journal of Cleaner Production*, 2022, 348: 9.
(42) Dong H.; Tang H.; Shi X.; Yang W.; Chen W.; Li H.; Zhao Y.; Zhang Z.; Hua M. Enhanced fluoride removal from water by nanosized cerium oxides impregnated porous polystyrene anion exchanger[J]. *Chemosphere*, 2022, 287: 131932.
(43) Yang W.; Shi X.; Dong H.; Tang H.; Chen W.; Wu M.; Hua M.; Zhang W. Fabrication of a reusable polymer-based cerium hydroxide nanocomposite with high stability for preferable phosphate removal[J]. *Chem Eng J*, 2021, 405: 126649.
(44) Liu R.; Chi L.; Wang X.; Wang Y.; Sui Y.; Xie T.; Arandiyan H. Effective and selective adsorption of phosphate from aqueous solution via trivalent-metals-based amino-MIL-101 MOFs[J]. *Chem Eng J*, 2019, (357): 159-168.
(45) Sriram G.; Thangarasu S.; Selvakumar K.; Kurkuri M.; Dhineshbabu N R.; Oh T H. Effective removal of Rose Bengal using Ni-Co-Zn layered triple hydroxide: Studies on batch adsorption, mechanism, selectivity, co-ions, and reusability[J]. *Colloids and Surfaces A: Physicochemical and Engineering Aspects*, 2024, 685: 133199.
(46) Sang W.; Mei L.; Hao S.; Li D.; Li X.; Zhang Q.; Jin X.; Li C. Na@ La-modified zeolite particles for simultaneous removal of ammonia nitrogen and phosphate from rejected water: performance and mechanism[J]. *Water Sci Technol*, 2020, 82(12): 2975-2989.
(47) Rajendran S.; Sai Bharadwaj A.; Barmavatu P.; Palani G.; Trilaksanna H.; Kannan K.; Meenakshisundaram N J C. A Review on Lanthanum-Based Materials for Phosphate Removal[J]. 2024, 8(1): 23.
(48) Angkawijaya A E.; Tran-Chuong Y N.; Ha Q N.; Tran-Nguyen P L.; Santoso S P.; Bundjaja V.; Go A W.; Hsu H-Y.; Ju Y-H. Studies on the performance of functionalized Fe_3O_4 as phosphate adsorbent and assessment to its environmental compatibility[J]. *Journal of the Taiwan Institute of Chemical Engineers*, 2022, 131: 104162.
(49) Angkawijaya A E.; Santoso S P.; Bundjaja V.; Soetaredjo F E.; Gunarto C.; Ayucitra A.; Ju Y-H.; Go A W.; Ismadji S. Studies on the performance of bentonite and its composite as phosphate adsorbent and phosphate supplementation for plant[J]. *J Hazard Mater*, 2020, 399: 123130.
(50) Jiang X.; Guan Q.; Feng M.; Wang M.; Yan N.; Wang M.; Xu L.; Gui Z. Preparation and pH controlled release of Fe_3O_4/anthocyanin magnetic biocomposites[J]. *Polymers*, 2019, 11(12): 2077.
(51) Andreas A.; Winata Z G.; Santoso S P.; Angkawijaya A E.; Yuliana M.;

Soetaredjo F E.; Ismadji S.; Hsu H-Y.; Go A W.; Ju Y-H. Biocomposite hydrogel beads from glutaraldehyde-crosslinked phytochemicals in alginate for effective removal of methylene blue[J]. *J Mol Liq*, 2021, 329: 115579.

(52) Huang W.; Jin Z.; Yang H.; Qu Y.; Che F.; Xu Z.; Dong J.; Wang K. Interception of phosphorus release from sediment by magnetite/lanthanum carbonate co modified activated attapulgite composite: Performance and mechanism[J]. *Colloids Surfaces A: Physicochemical Engineering Aspects*, 2023, (664): 131139.

(53) Xie N.; Yi L.; Li J.; Wang W.; Gu T.; Ma M-G.; Wang S.; Liu S. A green synthesis strategy toward calcined calcium-aluminum layered double hydroxide with sludge as aluminum source for efficient removal of phosphate from water[J]. *Surfaces Interfaces*, 2024, 46: 104075.

(54) Lin J.; Zhao Y.; Zhan Y.; Wang Y. Control of internal phosphorus release from sediments using magnetic lanthanum/iron-modified bentonite as active capping material[J]. *Environ Pollut*, 2020, 264: 114809.

(55) Niu J.; Ding P.; Jia X.; Hu G.; Li Z. Study of the properties and mechanism of deep reduction and efficient adsorption of Cr (VI) by low-cost Fe_3O_4-modified ceramsite[J]. *Sci Total Environ*, 2019, 688: 994-1004.

(56) Fan T.; Wang M.; Wang X.; Zha S. Experimental Study of the Adsorption of Nitrogen and Phosphorus by Natural Clay Minerals[J]. *Adsorption Science & Technology*, 2021.

(57) Li X.; Wen Q.; Chen J.; Sun W.; Zheng Y.; Long C.; Wang Q. Lanthanide molecular species generated Fe_3O_4@ SiO_2-TbDPA nanosphere for the efficient determination of nitrite[J]. *Molecules*, 2022, 27(14): 4431.

(58) He Q.; Zhao H.; Teng Z.; Wang Y.; Sun W.; Guo Y.; Ji X.; Hu W.; Lam S S.; Li M. Efficient recovery of phosphate by Fe_3O_4/La-MOF: An insight of adsorption performance and mechanism from electrochemical properties[J]. *Separation Purification Technology*, 2023, 314: 123529.

(59) Li S.; Jiang F.; Lei T.; Ren Z.; Wang S.; Yang X. Phosphorus removal by in situ sprayed ferric chloride in Dianchi Lake: Efficiency, stability, and mechanism[J]. *Process Safety and Environmental Protection*, 2019, 131: 320-328.